



**HAL**  
open science

# A First Look with JWST Aperture Masking Interferometry: Resolving Circumstellar Dust around the Wolf–Rayet Binary WR 137 beyond the Rayleigh Limit

Ryan M. Lau, Matthew J. Hankins, Joel Sanchez-Bermudez, Deepashri Thatte, Anthony Soulain, Rachel A. Cooper, Anand Sivaramakrishnan, Michael F. Corcoran, Alexandra Z. Greenbaum, Theodore R. Gull, et al.

► **To cite this version:**

Ryan M. Lau, Matthew J. Hankins, Joel Sanchez-Bermudez, Deepashri Thatte, Anthony Soulain, et al.. A First Look with JWST Aperture Masking Interferometry: Resolving Circumstellar Dust around the Wolf–Rayet Binary WR 137 beyond the Rayleigh Limit. *The Astrophysical Journal*, 2024, 963, 10.3847/1538-4357/ad192c . insu-04836893

**HAL Id: insu-04836893**

**<https://insu.hal.science/insu-04836893v1>**

Submitted on 13 Dec 2024

**HAL** is a multi-disciplinary open access archive for the deposit and dissemination of scientific research documents, whether they are published or not. The documents may come from teaching and research institutions in France or abroad, or from public or private research centers.

L'archive ouverte pluridisciplinaire **HAL**, est destinée au dépôt et à la diffusion de documents scientifiques de niveau recherche, publiés ou non, émanant des établissements d'enseignement et de recherche français ou étrangers, des laboratoires publics ou privés.



Distributed under a Creative Commons Attribution 4.0 International License



# A First Look with JWST Aperture Masking Interferometry: Resolving Circumstellar Dust around the Wolf–Rayet Binary WR 137 beyond the Rayleigh Limit

Ryan M. Lau<sup>1</sup>, Matthew J. Hankins<sup>2</sup>, Joel Sanchez-Bermudez<sup>3,4</sup>, Deepashri Thatte<sup>5</sup>, Anthony Soulain<sup>6</sup>, Rachel A. Cooper<sup>5</sup>, Anand Sivaramakrishnan<sup>5,7,8</sup>, Michael F. Corcoran<sup>9,10</sup>, Alexandra Z. Greenbaum<sup>11</sup>, Theodore R. Gull<sup>5,12</sup>, Yinuo Han<sup>13</sup>, Olivia C. Jones<sup>14</sup>, Thomas Madura<sup>15</sup>, Anthony F. J. Moffat<sup>16,17</sup>, Mark R. Morris<sup>18</sup>, Takashi Onaka<sup>19</sup>, Christopher M. P. Russell<sup>20</sup>, Noel D. Richardson<sup>21</sup>, Nathan Smith<sup>22</sup>, Peter Tuthill<sup>23</sup>, Kevin Volk<sup>5</sup>, Gerd Weigelt<sup>24</sup>, and Peredur M. Williams<sup>25</sup>

<sup>1</sup> NSF's NOIRLab, 950 N. Cherry Avenue, Tucson, AZ 85719, USA; [ryan.lau@noirlab.edu](mailto:ryan.lau@noirlab.edu)

<sup>2</sup> Arkansas Tech University, 215 West O Street, Russellville, AR 72801, USA

<sup>3</sup> Instituto de Astronomía, Universidad Nacional Autónoma de México, Apdo. Postal 70264, Ciudad de México 04510, Mexico

<sup>4</sup> Max-Planck-Institut für Astronomie, Königstuhl 17, D-69117 Heidelberg, Germany

<sup>5</sup> Space Telescope Science Institute, 3700 San Martin Drive, Baltimore, MD 21218, USA

<sup>6</sup> Université Grenoble Alpes, CNRS, IPAG, 38100 Grenoble, France

<sup>7</sup> Astrophysics Department, American Museum of Natural History, 79th Street at Central Park West, New York, NY 10024, USA

<sup>8</sup> Department of Physics and Astronomy, Johns Hopkins University, 3701 San Martin Drive, Baltimore, MD 21218, USA

<sup>9</sup> CRESST II and X-ray Astrophysics Laboratory NASA/GSFC, Greenbelt, MD 20771, USA

<sup>10</sup> Institute for Astrophysics and Computational Sciences, The Catholic University of America, 620 Michigan Avenue, N.E. Washington, DC 20064, USA

<sup>11</sup> IPAC, California Institute of Technology, 1200 E. California Boulevard, Pasadena, CA 91125, USA

<sup>12</sup> Code 667, NASA/GSFC, Greenbelt, MD 20771, USA

<sup>13</sup> Institute of Astronomy, University of Cambridge, Madingley Road, Cambridge CB3 0HA, UK

<sup>14</sup> UK Astronomy Technology Centre, Royal Observatory, Blackford Hill, Edinburgh EH9 3HJ, UK

<sup>15</sup> Department of Physics and Astronomy, San Jose State University, San Jose, CA, USA

<sup>16</sup> Département de Physique, Université de Montréal, C.P. 6128, succ. centre-ville, Montréal (Qc) H3C 3J7, Canada

<sup>17</sup> Centre de Recherche en Astrophysique du Québec, Canada

<sup>18</sup> Department of Physics and Astronomy, University of California, Los Angeles, 430 Portola Plaza, Los Angeles, CA 90095-1547, USA

<sup>19</sup> Department of Astronomy, School of Science, University of Tokyo, 7-3-1 Hongo, Bunkyo-ku, Tokyo 113-0033, Japan

<sup>20</sup> Department of Physics and Astronomy, Bartol Research Institute, University of Delaware, Newark, DE 19716, USA

<sup>21</sup> Department of Physics and Astronomy, Embry-Riddle Aeronautical University, 3700 Willow Creek Road, Prescott, AZ 86301, USA

<sup>22</sup> Steward Observatory, 933 North Cherry Avenue, Tucson, AZ 85721, USA

<sup>23</sup> School of Physics, The University of Sydney, NSW 2006, Australia

<sup>24</sup> Max-Planck-Institut für Radioastronomie, Auf dem Hügel 69, D-53121 Bonn, Germany

<sup>25</sup> Institute for Astronomy, University of Edinburgh, Royal Observatory, Edinburgh EH9 3HJ, UK

Received 2023 August 4; revised 2023 November 15; accepted 2023 November 16; published 2024 March 6

## Abstract

We present infrared aperture-masking interferometry (AMI) observations of newly formed dust from the colliding winds of the massive binary Wolf–Rayet system WR 137 with JWST using the Near Infrared Imager and Slitless Spectrograph (NIRISS). NIRISS AMI observations of WR 137 and a point-spread function calibrator star, HD 228337, were taken using the F380M and F480M filters in 2022 July and August as part of the Director's Discretionary Early Release Science program #1349. Interferometric observables (squared visibilities and closure phases) from the WR 137 “interferogram” were extracted and calibrated using three independent software tools: ImPlaneIA, AMICAL, and SAMpip. The analysis of the calibrated observables yielded consistent values except for slightly discrepant closure phases measured by ImPlaneIA. Based on all three sets of calibrated observables, images were reconstructed using three independent software tools: BSMEM, IRBis, and SQUEEZE. All reconstructed image combinations generated consistent images in both F380M and F480M filters. The reconstructed images of WR 137 reveal a bright central core with a  $\sim 300$  mas linear filament extending to the northwest. A geometric colliding-wind model with dust production constrained to the orbital plane of the binary system and enhanced as the system approaches periastris provided a general agreement with the interferometric observables and reconstructed images. Based on a colliding-wind dust condensation analysis, we suggest that dust formation within the orbital plane of WR 137 is induced by enhanced equatorial mass loss from the rapidly rotating O9 companion star, whose axis of rotation is aligned with that of the orbit.

*Unified Astronomy Thesaurus concepts:* Circumstellar dust (236); WC stars (1793); High contrast techniques (2369); James Webb Space Telescope (2291); Massive stars (732)

*Supporting material:* data behind figures

## 1. Introduction

Classical Wolf–Rayet (W-R) stars, the descendants of massive OB-type stars, are characterized by high luminosities ( $L_* \gtrsim 10^5 L_\odot$ ), hot surface temperatures ( $T_* \gtrsim 40,000$  K), and fast, powerful winds ( $v_\infty \gtrsim 1000$  km s<sup>-1</sup>,  $\dot{M} \gtrsim 10^{-5.5} M_\odot$  yr<sup>-1</sup>;

Crowther 2007; Hamann et al. 2019; Sander et al. 2019). The high luminosities and intense UV radiation produced by W-R stars may present an inhospitable environment for dust grains; however, IR observations have demonstrated that a subset of W-R stars exhibits dust production (e.g., Allen et al. 1972; Williams 2019; Lau et al. 2020a). These dust-producing objects have enhanced carbon abundances (WC stars) and come in two categories: ones that continuously produce dust and those that produce dust in an episodic fashion (Williams et al. 1987). For the majority of these objects, the dust-formation process is thought to be tied to their binary nature, where a collision between the WC star wind and that of an OB-type companion produces high densities and efficient cooling that favor dust formation (e.g., Usov 1991). However, the detailed physics of colliding-wind dust production is not well understood, and much of our present knowledge has been gleaned from periodic dust producers whose dust-formation episodes have been directly tied to the binary orbit. The archetypical example of this is WR 140, which produces dust like clockwork during its periastron passage every 7.93 yr (Williams et al. 2009; Lau et al. 2022).

WR 137 (also known as HD 192641) is another well-known dust-producing WC binary which shows repeating dust-formation events (Williams et al. 1985, 2001). It is a confirmed binary consisting of a WC7 star and an O9e-type companion (St-Louis et al. 2020), and has a measured orbital period of 13.1 yr (Lefèvre et al. 2005). The IR light curve of WR 137 exhibits high-amplitude ( $\gtrsim 1$  mag) IR brightening episodes with a similar cadence to the orbital period of the binary (Williams et al. 2001), which suggests that dust formation is orbitally modulated as in WR 140. However, previous images of WR 137 taken in the near-infrared by the Hubble Space Telescope (HST) present compact, “jet-like” dust emission (Marchenko et al. 1999) that does not resemble any of the other known dust-forming WC binary systems (Tuthill et al. 1999; Monnier et al. 2007; Lau et al. 2020b). Investigating the connection between WR 137’s dust formation and its orbital properties has been challenging due to the compact morphology of its extended dust emission. Observations with high spatial resolution, high imaging contrast, and high sensitivity at mid-infrared wavelengths are therefore essential for resolving and characterizing the nature of the faint extended dust emission around WR 137.

As part of Director’s Discretionary Early Release Science (DD-ERS) program #1349, WR 137 was selected as a target to investigate colliding-wind dust formation and to demonstrate the scientific potential of the aperture-masking interferometry (AMI) mode of Near Infrared Imager and Slitless Spectrograph (NIRISS). The seven-hole, nonredundant AMI pupil mask is shown in Figure 1 (upper left) overlaid on an outline of the JWST primary mirror. Although the usage of the nonredundant mask (NRM) that enables AMI<sup>26</sup> on NIRISS to block  $\sim 85\%$  of the incoming light (Artigau et al. 2014), AMI techniques provide angular resolution that is  $\sim 2\times$  higher compared to traditional imaging (i.e.  $\sim 0.5\lambda/D$ ). This facilitates studies of small-angular-scale dust features near a bright point source.

Previously, AMI has been used on large, ground-based telescopes to study the size and morphology of several dusty W-R stars at IR wavelengths (see, e.g., Tuthill et al. 1999; Monnier et al. 2007; Rajagopal et al. 2007; Hankins et al. 2016).

JWST/NIRISS AMI, operating at a temperature of 40 K, brings advantages of space-based interferometry at these wavelengths: about an order of magnitude better fringe-phase measurements, which are sensitive to the point-antisymmetrical component of the target; 2 or 3 orders of magnitude better fringe amplitude calibration that track symmetrical target structure; and much lower thermal background than high-resolution, ground-based telescopes (Sivaramakrishnan et al. 2009, 2023). Notably, revealing diffuse extended components such as disks or rings is challenging from the ground because fringe amplitudes are often corrupted by atmospheric scintillation. JWST has therefore opened a new window of AMI observations from space and enables investigations that require high spatial resolution at mid-infrared wavelengths and greater sensitivity to extended structures.

In this paper, we present JWST/NIRISS AMI observations of WR 137 using the F380M and F480M filters. The timing of the observations was planned to align with active dust formation from WR 137 based on its IR light curve and known spectroscopic orbit (Williams et al. 2001; Lefèvre et al. 2005; Peatt et al. 2023). In Section 2, we describe the observations, preparation, data reduction, and the procedures used to extract interferometric observables from the NIRISS AMI data. In Section 3, we present reconstructed images of WR 137 using three different image reconstruction software packages which we then analyze and compare with geometric dust models used to study other dust-forming WC binaries (e.g., Han et al. 2022). Lastly, in Section 4, we discuss WR 137’s dust morphology and the possible influence of its rapidly rotating companion star on conditions for dust formation via wind–wind collision.

## 2. Observations and Data Reduction

### 2.1. JWST/NIRISS AMI Observations, Preparation, and Data Reduction

JWST observations of WR 137 were carried out as part of DD-ERS program #1349 (PI: R. Lau) and were obtained using the AMI mode of the NIRISS instrument (Doyon et al. 2023; Sivaramakrishnan et al. 2023). Observations of WR 137 and a PSF calibrator star (HD 228337) were taken using the F380M ( $\lambda_{\text{pivot}} = 3.825 \mu\text{m}$ ;  $\Delta\lambda = 0.205 \mu\text{m}$ ) and F480M ( $\lambda_{\text{pivot}} = 4.815 \mu\text{m}$ ;  $\Delta\lambda = 0.298 \mu\text{m}$ ) filters on 2022 July 13 and 15, and 2022 August 9.

The NIRISS AMI observations used the standard AMI parameters with the “NISRAPID” readout pattern and the SUB80 ( $80 \times 80$  pixel) subarray, where the NIRISS detector plate scale is  $65 \text{ mas pixel}^{-1}$  and the readout time is 75.44 ms. The total (effective) exposure times of the F480M and F380M observations of WR 137 were 10.6 (8.0) and 11.2 (6.8) minutes, respectively. The total exposure time of the PSF calibrator is identical to that of WR 137. Details of the observations can be found in Table 1. For both WR 137 and the PSF calibrator, target acquisition was used on the same target as the observation in the “AMIBRIGHT” acquisition mode with the F480M filter and five groups in the NISRAPID readout pattern. NIRISS AMI observations also allow for direct imaging using the “CLEARP” aperture with the same filters and subarray used for the AMI exposures. Direct F380M and F480M images of WR 137 were therefore obtained with the AMI exposures on 2022 July 15. The total (effective) exposure times of the direct F480M and F380M observations were 39.7 (31.7) and 39.5 (24.1) s, respectively. However, as expected

<sup>26</sup> Also referred to as sparse aperture masking.

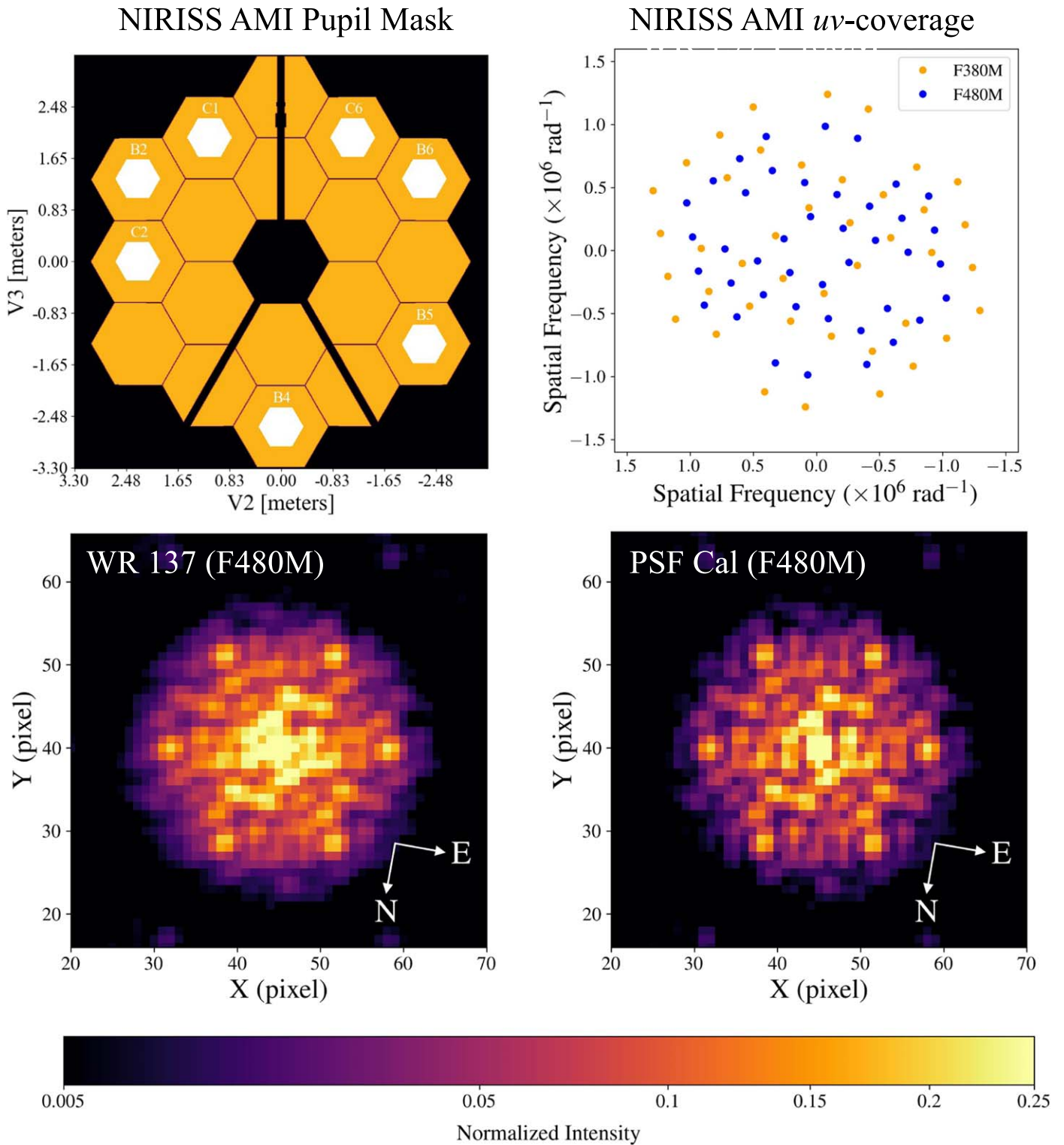


**Figure 1.** Upper left: the seven-hole nonredundant NIRISS AMI pupil mask (white hexagons) overlaid on an outline of the JWST primary mirror. Upper right: the  $u-v$  plane coverage of the nondithered F380M and F480M observations of WR 137. Bottom left:  $50 \times 50$  pixel cutout centered on the interferogram pattern produced by the seven-hole NRM on the  $80 \times 80$  pixel SUB80 subarray for WR 137 and the point-spread function (PSF) calibrator star (bottom right), both with the F480M filter. The images displayed are a median of frames that have gone through both stage 1 and 2 processing, and are shown with a normalized power-law stretch (index = 0.5). Each pixel corresponds to 65 mas and the color bar corresponds to intensity normalized to the peak pixel value. Although subtle, the WR 137 interferogram pattern appears to have a lower contrast than the PSF calibrator interferogram. This is the result of structure other than the bright central compact source and therefore indicates the presence of resolved emission around WR 137.

due its brightness, the PSF core of WR 137 was saturated in both filters and was therefore not used for the analysis in this paper.

In preparation for the observations, simulated NIRISS AMI data products of WR 137 and PSF calibrator HD 228337 were generated to ensure the success of the AMI observing strategy.

**Table 1**  
Summary of Observations

Obs. Date	Object	Filter	Obs. Type	NGROUPS	NINTS	Dither Pattern
2022-07-15 13:37:18.246	WR 137	F480M	NRM/SUB80	4	1600	Stare
2022-07-15 13:37:17.634	WR 137	F380M	NRM/SUB80	2	2720	Stare
2022-07-15 12:12:59.178	HD 228337	F480M	NRM/SUB80	7	1020	Stare
2022-07-15 12:20:57.815	HD 228337	F380M	NRM/SUB80	2	2720	Stare
2022-07-13 12:43:39.770	WR 137	F480M	NRM/SUB80	4	400	Four-point
2022-07-13 12:43:37.531	WR 137	F380M	NRM/SUB80	2	680	Four-point
2022-08-9 17:33:05.182	WR 137	F480M	NRM/SUB80	4	400	Four-point
2022-08-9 17:33:00.515	WR 137	F380M	NRM/SUB80	2	680	Four-point
2022-08-9 17:51:33.502	HD 228337	F480M	NRM/SUB80	7	255	Four-point
2022-08-9 17:33:45.279	HD 228337	F380M	NRM/SUB80	2	680	Four-point

**Note.** Summary of the JWST/NIRISS AMI observations of WR 137 and the PSF calibrator HD 228337. All AMI observations were taken using the NIRISS NRM in the SUB80 subarray, which is standard for the AMI mode. NGROUPS and NINTS correspond to the number of groups per integration and the number of integrations per exposure, respectively. Observations using two different dither patterns, stare and four-point, were performed with identical total exposure times. Note that a duplicate set of dithered data of WR 137 exists because PSF calibrator observations that were planned to follow the July 13 observations of WR 137 were skipped due to a mirror “tilt event.” The set of WR 137 and PSF calibrator observations were successfully completed on August 9.

The Multi-Instrument Ramp Generator (MIRaGe; Hilbert et al. 2022) was used to simulate raw NIRISS AMI data in the F380M and F480M filters. MIRaGe simulations utilized the Astronomer’s Proposal Tool (APT) file for DD-ERS #1349, a simulated sky scene of WR 137, and a source catalog with the flux densities of HD 228337 to generate raw exposures identical to the observing configuration specified in the APT file. The simulated raw exposures were then processed through the same procedures, described further in this section, as were performed on the real data. The simulated reduced data products demonstrate that the NIRISS AMI observing configuration described above is capable of detecting the predicted extended dust emission near WR 137 (Marchenko et al. 1999; Williams et al. 2001).

Due to WR 137’s brightness in the mid-infrared ( $F_{3.8\ \mu\text{m}} \gtrsim 1\ \text{Jy}$ ; Williams et al. 2001), it was important that the number of groups used per integration (NGROUPS) in the observations be specified to avoid nonlinearity effects. Charge migration, also known as the “brighter–fatter effect” (Hirata & Choi 2020), is of particular concern for AMI data and occurs due to the buildup of a transverse electric field as charge accumulates in sufficiently illuminated pixels (e.g., Coulton et al. 2018). This effect can significantly impact AMI data given that the core of the PSF contains critical information about the structure of the source.

Commissioning tests indicated that charge migration between the brightest pixel at the center of an image of an unresolved star and its eight neighboring pixels remained below 1% as long as the peak pixel’s accumulated up-the-ramp charge remained below 30,000 electrons, the nominal saturation limit for the AMI mode (Sivaramakrishnan et al. 2023). Sampling up the ramp with sufficient NGROUPS allows the count rate in the peak pixel and surrounding pixels to be examined as a function of exposure time by processing sections of each integration in an exposure as if they were independent exposures. Observations of WR 137 with NGROUPS = 4 and the PSF calibrator star with NGROUPS = 7 were examined in this way and found to display nonlinearity due to charge migration of at most 2% at the highest signal level reached. The impact of charge migration on our data set is therefore negligible.

Two sets of observations with identical exposure times were obtained using different dither patterns in order to investigate the optimal dither pattern for the NIRISS AMI mode. The two modes used were a nondithered “stare” mode and a four-point dither pattern with four primary dithers. Although further work is planned for a more detailed investigation of dither versus stare mode, the stare observations are used for the analysis in this paper because of larger uncertainties in the interferometric observables extracted from the dithered observations. Figure 1 (upper right) shows the  $u$ – $v$  plane coverage of the nondithered F380M and F480M observations and presents the spatial frequencies sampled by the NRM. A duplicate set of dithered data of WR 137 exists (Table 1) because PSF calibrator observations that were supposed to be taken following the July 13 observations of WR 137 were skipped due to a mirror “tilt event” (Rigby et al. 2023). The set of WR 137 and PSF calibrator observations using the four-point primary dithers was rescheduled for August 9 and successfully completed.

The observations of WR 137 and the PSF calibrator were reduced using version 1.11.2 of the standard JWST science calibration pipeline with version 11.17.2 of the Calibration Reference Data System for stage 1 and 2 processing. The raw data were first passed to the *calwebb\_detector1* routine (stage 1), a series of detector-level processing steps which take individual integrations and produce a corrected count rate image. The data were then passed to the *calwebb\_image2* routine (stage 2), which performs instrumental corrections and calibrations on the count rate images to produce fully calibrated exposures.

Figure 1 (bottom) presents a cutout of the “interferogram” patterns from the calibrated, nondithered F480M exposures of WR 137 and the PSF calibrator. Since the mask holes are not obstructed by any mirror struts or mirror segment edges (Figure 1, upper left), the holes share the same PSF envelope or “primary beam” shape. This primary beam is modulated by the interferometric fringe pattern generated by the baselines between pairs of holes (see Greenbaum et al. 2015). The hexagonal hole shape leads to the overall hexagonal shape of the interferogram. The core of the WR 137 interferogram appears more extended than the PSF calibrator, which indicates the presence of resolved emission around WR 137. This extended emission in the core of the WR 137 interferogram is

a result of reduced fringe amplitudes caused by structure other than the bright central compact source. The more-or-less isotropic nature of the extended emission results from additional structures in various directions from the dominant compact source. For example, if the target were instead a moderate contrast binary the image would look extended along the two components' separation vector. In the case of WR 137, structure clearly extends more than a resolution element from the compact bright source. Note that fringe-phase information is difficult to see directly from the interferogram and requires additional tools for extraction.

## 2.2. Extracting Interferometric Observables with ImPlaneIA, SAMpip, and AMICAL

The final stage of NIRISS AMI data processing (stage 3) includes the extraction of interferometric observables (squared visibilities and closure phases) from the calibrated exposures. Details of this process are described in Sivaramakrishnan et al. (2023). At the time of this work, the third stage did not use the JWST science calibration pipeline for NIRISS AMI data. The stage 3 processing tasks were conducted using three independent software packages: ImPlaneIA<sup>27</sup> (Greenbaum et al. 2015, 2018), SAMpip (Sanchez-Bermudez et al. 2022), and AMICAL (Soullain et al. 2020; Soullain & Robert 2023). Comparing the results across the three software tools was important for ensuring robust measurements given that observable extraction of AMI data has had limited testing with space-based observations. For each software tool, measured observables for the science target (WR 137) were extracted and then calibrated using the observables of the PSF calibration source (HD 228337).

There is an important detail to be noted about the data processing related to cosmic-ray events. In the version of the JWST science pipeline used on this data set, cosmic-ray events are flagged at stage 1 (jump detection step); however, this did not apply to observations with NGROUPS fewer than 3. The F380M observations for this program, where NGROUPS = 2, notably do not meet this requirement and so data impacted by cosmic rays were passed on to the stage 3 processing steps. The presence of cosmic rays can present issues with the image plane algorithms (ImPlaneIA and SAMpip).

All three software tools (ImPlaneIA, SAMpip, and AMICAL) extract interferometric observables from each integration and deliver the raw weighted mean and standard deviation in a final Optical Interferometry Flexible Image Transport System (OIFITS; Pauls et al. 2005; Duvert et al. 2017) file. SAMpip and ImPlaneIA create a model of the data by fitting the fringes directly in the image plane, and the interferometric observables are derived from the model's coefficients. AMICAL instead computes the Fourier transform of the interferogram and locates the position of the different spatial frequencies (and their corresponding visibility amplitudes and phases) using a matched filter template with the mask's geometry. Detailed information on the application of ImPlaneIA, SAMpip, and AMICAL to NIRISS AMI data is provided in Section 5.3 of Sivaramakrishnan et al. (2023).

Lastly, calibrating out the instrumental transfer function of the squared visibilities is done by dividing the raw observables of the target by those of the calibrator star, and the calibration

of the closure phases is done by subtracting the closure phases of the calibrator from those of the target. Figure 2 shows the resulting calibrated interferometric observables for the science target with all three softwares using both the F380M and F480M observations. The calibrated squared visibilities derived from all three softwares are in close agreement, as are the calibrated closure phases from AMICAL and SAMpip. The cause for the discrepant closure phases derived from ImPlaneIA in both F380M and F480M observations is currently under investigation by the ImPlaneIA development team. The discrepancy appears to be due to a difference in the ways ImPlaneIA and SAMpip compute the statistics of interferometric variables. ImPlaneIA determines errors in fringe phases, and separately, fringe amplitudes. SAMpip calculates statistics using fringe complex visibilities before converting the complex errors into real number fringe phase and amplitude errors. ImPlaneIA is currently being updated to use complex visibility averages, which will likely bring it into alignment with SAMpip's error estimation. The SAMpip and ImPlaneIA teams are working to quantify the effect of differences in the computed observables' statistics.

## 3. Results and Analysis

### 3.1. Image Reconstruction of WR 137's Circumstellar Environment

F380M and F480M images of WR 137 were reconstructed from the calibrated observables (Figure 2) using three different software tools: BSMEM (Buscher 1994; Lawson et al. 2004), SQUEEZE (Baron et al. 2010), and IRBis (Hofmann et al. 2014). Each of the image reconstruction software tools was applied to the three sets of calibrated observables extracted by ImPlaneIA, AMICAL, and SAMpip. The reconstructed F380M and F480M images are presented in Figures 3 and 4, respectively. This threefold approach provides independent methods of processing NIRISS AMI data and performing image reconstruction. The angular resolution achieved in these reconstructed images is  $\sim 0.5\lambda/D$ , which corresponds to  $\sim 60$  and  $\sim 80$  mas for the F380M and F480M observations, respectively. An absolute photometric calibration was not performed on the reconstructed images due to the saturation of WR 137 in the direct NIRISS images (Section 2.1). However, future work is planned on strategies for performing an absolute photometric calibration of AMI observations targeting bright sources (e.g., utilizing the PSF reference star).

For each reconstructed image, similar image sizes and pixel scales corresponding to  $128 \times 128$  pixels and  $7.42 \text{ mas pixel}^{-1}$ , respectively, were adopted. For the SQUEEZE reconstruction we employed entropy regularization and performed a simple grid search for a suitable hyperparameter value in the range from  $\mu = 10^{-3}$  to  $\mu = 10^3$  in logarithmic steps. For regularized minimization algorithms, the hyperparameter is a user-defined parameter that balances the weight between the likelihood and the prior probabilities when estimating the best-fit image. The best-fit values for the hyperparameters were found with  $\mu \leq 10^{-1}$  with minimal variation in the range of  $\mu = 10^{-3}$ – $10^{-1}$ . Figures 3 and 4 present reconstructed images with hyperparameters of  $\mu = 10^{-2}$ . The final SQUEEZE results presented are generated from an average of model chains which achieve a reduced chi-squared value  $\chi_r^2 \lesssim 1.5$ . The BSMEM reconstruction automatically selects the hyperparameter for the reconstruction. This software uses entropy as its regularization

<sup>27</sup> <https://github.com/anand0xff/ImPlaneIA/commit/b6caf9db3b6976b3427b2a4ce5798e470f022c3d>

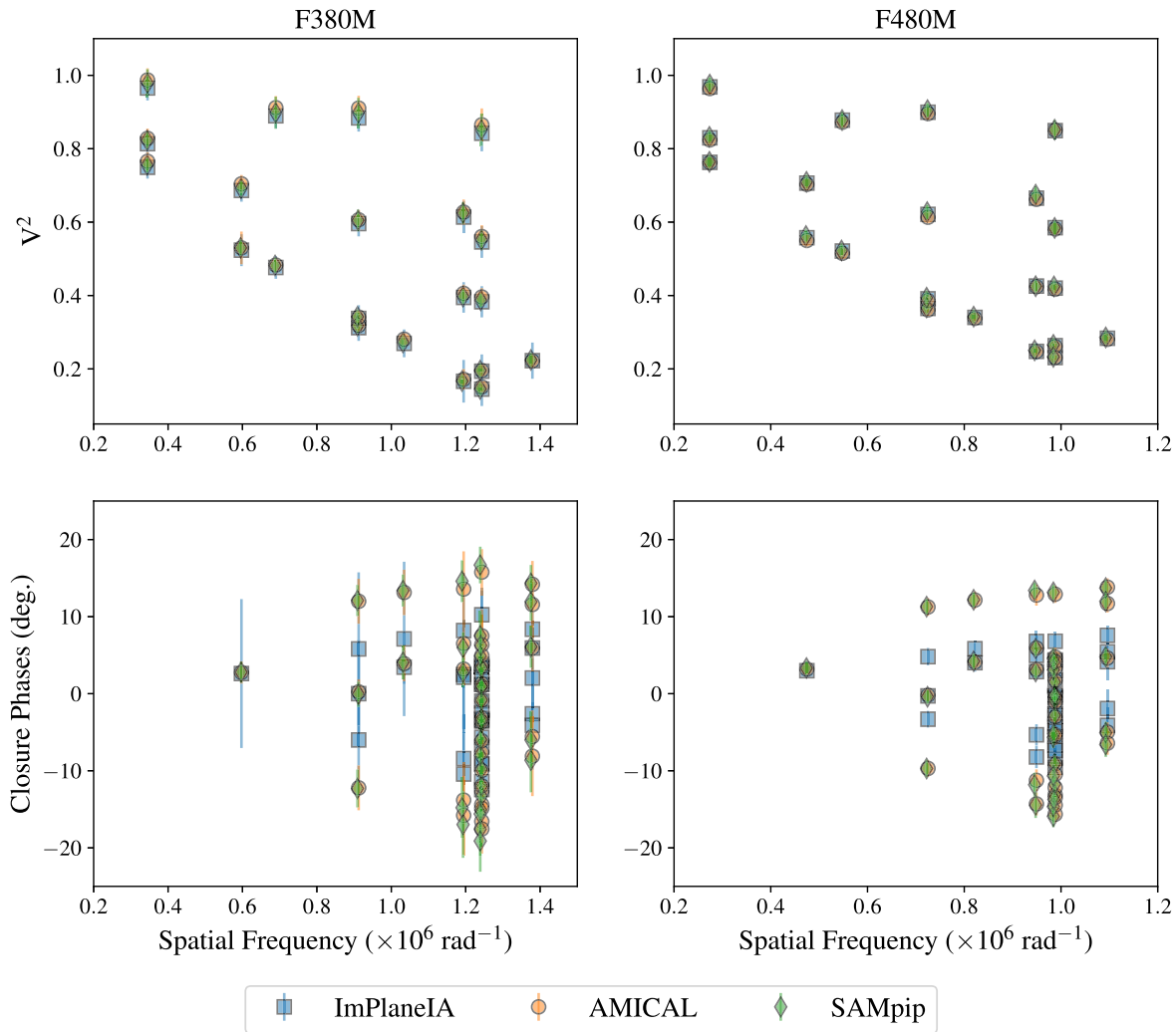


**Figure 2.** Calibrated Interferometric observables extracted from the WR 137 observations using ImPlaneIA, AMICAL, and SAMpip. These data include calibrated squared visibilities ( $V^2$ ; top) and closure phases (bottom) for the F380M (left) and F480M (right) filters. The data behind these panels are available in six OIFITS files in the .tar.gz package.

(The data used to create this figure are available.)

function, which tends to produce smooth brightness distributions. Furthermore, the entropy regularizer ensures that the pixel values are always positive. The  $\chi_r^2$  values obtained are close to unity.

For IRBis, the image was reconstructed using the edge-preserving regularization function. An additional mask was also utilized to use only the flux within the mask radius  $r_{\text{mask}}$ . The reconstruction was then performed using a combination of  $\mu$  ( $0.1\text{--}10^{-5}$ ) and  $r_{\text{mask}}$  (550–640 mas). The prior image was a Gaussian model with an FWHM of 650 mas. The best reconstructed image was finally selected using the reconstruction quality parameters  $q_{\text{rec}}$  based on the  $\chi_r^2$  and the residual ratio values  $\rho\rho$  (see Hofmann et al. 2014). The final IRBis results provided good agreement with the data for both F380M and F480M filters. The IRBis results also presented a systematically better fit for the closure phases than the visibility amplitude.

Figures 3 and 4 demonstrate that all combinations of image reconstruction tool and observable extraction software produce similar reconstructed images of WR 137 at both wavelengths.

The dust emission extending to the NW from WR 137 appears quasi linear with some slight curvature angled to the north. The extent of the linear emission is slightly shorter in the F380M images ( $\sim 200$  mas) compared to the F480M images ( $\sim 300$  mas). The detection of more extended emission in the F480M images is likely due to lower uncertainties in the F480M observables (Figure 2) and/or cooler dust temperatures at larger distances along the feature. NIRISS AMI performance may be better in the F480M data than the F380M data because the 65 mas detector pixels better sample the F480M data than the shorter-wavelength F380M data. The faint structure extending to the southeast, which is most prominent in the IRBis reconstructions of the ImPlaneIA observables, is unlikely real given the absence of this feature in all other image reconstructions. The appearance of the southeast extension only in images reconstructed from the ImPlaneIA-calibrated observables is likely due to the slightly discrepant closure phase measurements (Figure 2).

A comparison of real astrophysical features and likely artifacts from the image reconstruction is presented in Figure 5, which shows the BSMEM-reconstructed image data from the

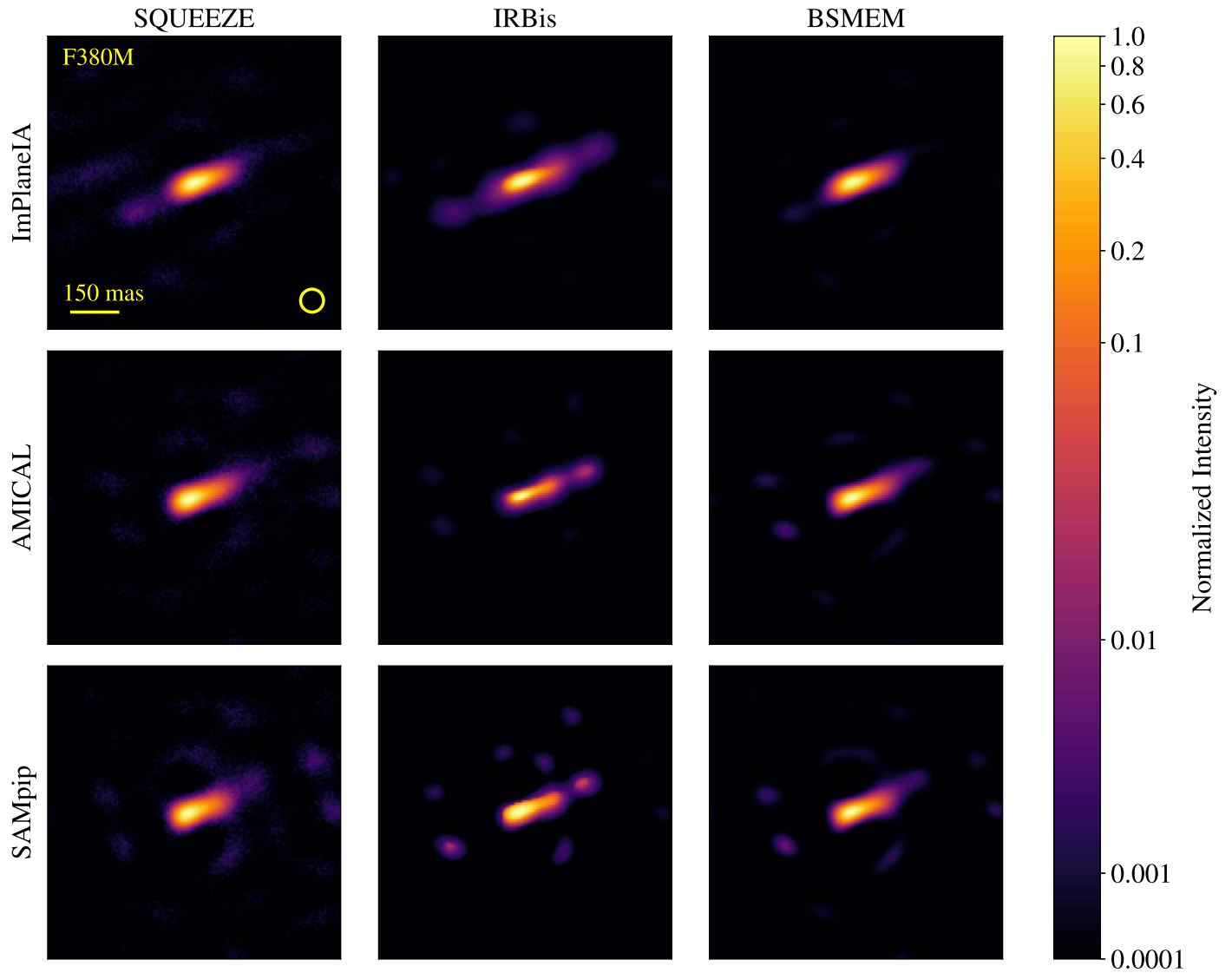


**Figure 3.** SQUEEZE, IRBis, and BSMEM image reconstructions of WR 137 based on the calibrated observables from the NIRISS AMI F380M observations extracted by ImPlaneIA, AMICAL, and SAMpip. All images are shown with a logarithmic stretch normalized to the peak pixel intensity. The normalized intensity color bar is shown on the right. The angular resolution of the F380M images is indicated by the yellow circles in the upper left panel and corresponds to 60 mas. In all panels, north is up and east is to the left. The data behind these panels are available in nine FITS image files in the .tar.gz package.

(The data used to create this figure are available.)

F380M and F480M observables extracted by SAMpip. While the overlapping F380M and F480M emission of the bright, linear feature traces astrophysical emission from dust, the faint elliptical features that are displaced in radial position between the F380M and F480M images are most likely image reconstruction artifacts.

The linear extended emission in the reconstructed images resembles previous observations of WR 137 obtained by ground-based mid-infrared imaging (Marchenko & Moffat 2007). The orientation of this feature is also consistent with the alignment of dust clumps revealed by near-infrared imaging with HST (Marchenko et al. 1999), which were obtained at a slightly later orbital phase ( $\varphi \sim 0-0.06$ ) than the NIRISS observations ( $\varphi = 0.9$ ). The near-infrared clumps therefore likely trace dust density enhancements along a continuous, linear feature consistent with the feature revealed in the NIRISS observations. A shorter linear emission feature resolved in the

near-infrared HST images, however, extends in the opposite direction (southeast) of the NIRISS feature. If the origin of this feature is linked to colliding stellar winds (see Section 3.3), the opposite orientation is likely due to the different orbital configurations of the colliding-wind binary between the NIRISS and HST observations.

### 3.2. Colliding-wind Shock Opening Angle Analysis

The linear morphology of WR 137’s extended emission is different from the extended dust emission morphologies resolved around other dust-forming colliding-wind binaries (Tuthill et al. 1999; Monnier et al. 2007; Lau et al. 2020b). Such systems typically show structures consistent with dust formed in a hollow conical wind-collision region revolving with the stars in their orbit and symmetrical about their line of centers. The conical shape of the “shock cone” assumes the collision of two isotropic winds, and its opening angle depends on the wind-momentum



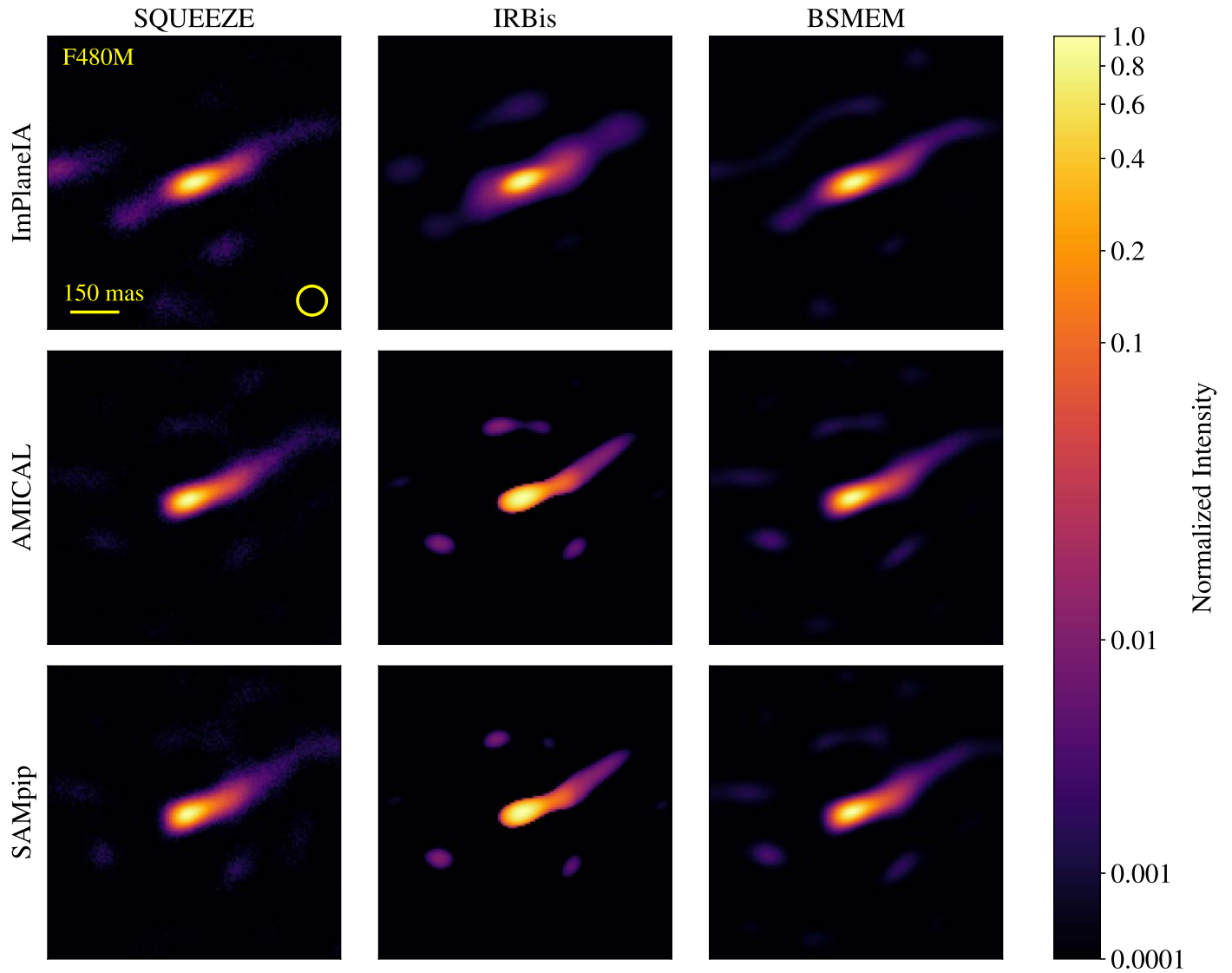


**Figure 4.** SQUEEZE, IRBis, and BSMEM image reconstructions of WR 137 based on the calibrated observables from the NIRISS AMI F480M observations extracted by ImPlaneIA, AMICAL, and SAMpip. All images are shown with a logarithmic stretch normalized to the peak pixel intensity. The normalized intensity color bar is shown on the right. The angular resolution of the F480M images is indicated by the yellow circles in the upper left panel and corresponds to 80 mas. In all panels, north is up and east is to the left. The data behind these panels are available in nine FITS image files in the .tar.gz package.

(The data used to create this figure are available.)

balance of the two stars (e.g., Usov 1991; Cantó et al. 1996). Assuming a purely hydrodynamic balance and spherically symmetric winds from the stars in WR 137, the half-opening angle of the thin shock cone ( $\theta_h$ ), appropriate for radiative postshock plasma, can be derived from the following expression (see Cantó et al. 1996; Tuthill et al. 2008):

$$\tan \theta_h - \theta_h = \frac{\eta \pi}{1 - \eta}, \quad (1)$$

where  $\eta$  is the wind-momentum ratio of the companion star and the W-R star:

$$\eta = \frac{\dot{M}_{\text{OB}} v_{\text{OB}}}{\dot{M}_{\text{WR}} v_{\text{WR}}}. \quad (2)$$

A shock-cone half-opening angle of  $\theta_h = 18^\circ.6$ , where  $\eta = 0.0038$ , can be derived from the mass-loss rates and terminal wind velocities of the two stars in WR 137 inferred from Potsdam

Wolf-Rayet (PoWR; Hamann & Gräfener 2004) models presented by Richardson et al. (2016):  $\dot{M}_{\text{WR}} = 10^{-4.65} M_\odot \text{ yr}^{-1}$ ,  $v_{\text{WR}} = 1700 \text{ km s}^{-1}$ ,  $\dot{M}_{\text{OB}} = 10^{-7.1} M_\odot \text{ yr}^{-1}$ , and  $v_{\text{OB}} = 1800 \text{ km s}^{-1}$ .

If the dust emission around WR 137 traces the entire surface of its shock cone, an upper limit of  $\sim 8^\circ$  for the shock-cone half-opening angle can be derived based on the extent of the linear emission and the angular resolution,  $\sim 300 \text{ mas}$  and  $80 \text{ mas}$ , respectively, for the F480M observations. The linear morphology of the extended emission from WR 137 therefore does not appear to be consistent with the predicted  $18^\circ.6$  half-opening angle. However, other factors can affect the dust morphology from colliding-wind binaries: the OB/WR wind-momentum ratio  $\eta$  may be overestimated, or the wind(s) may not be spherically symmetric thus leading to nonuniform dust formation across the surface of a possibly asymmetric shock cone. Since it is difficult to produce such a linear morphology even with a much smaller  $\eta$ , it is unlikely the morphology is

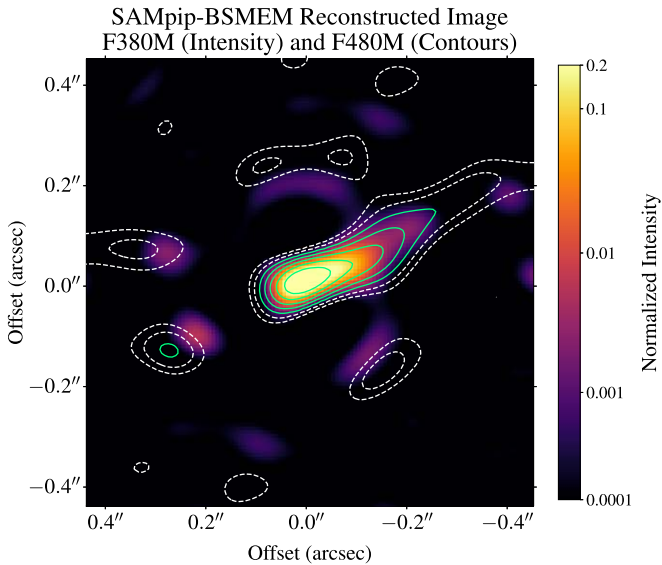


**Figure 5.** Reconstructed F380M (intensity) and F480M (contours) images of WR 137 using BS MEM on the observables extracted by SAMPip. The dashed, white contour levels correspond to normalized F480M intensities of  $10^{-3.5}$  and  $10^{-3.0}$ , and the green, solid contours levels correspond to  $10^{-2.5}$ ,  $10^{-2.0}$ ,  $10^{-1.5}$ ,  $10^{-1}$ , and  $10^{-0.5}$ . The  $\lesssim 10^{-2.5}$  features indicated by the dashed, white contours outside of the linear emission from WR 137 are likely not real given the wavelength dependence of their position.

solely due to an overestimate of  $\eta$ . For example, even if  $\eta$  were overestimated by a factor of 10, the full opening angle would be  $\sim 17^\circ$  and would be resolvable in the reconstructed images. The impact of wind asymmetries is particularly important to consider given the likely presence of a decretion disk around the O9 companion (St-Louis et al. 2020). Variable dust formation across the surface of the shock interface is therefore investigated in Section 3.3 utilizing a geometric colliding-wind modeling tool.

### 3.3. Interpreting WR 137’s Extended IR Emission with Geometric Colliding-wind Models

Geometric modeling of dust production from colliding-wind binaries provides an important tool to interpret the spatially resolved dust emission around dust-forming WC binaries (Williams et al. 2009; Callingham et al. 2019; Han et al. 2022; Lau et al. 2022). Such models, which output a map of dust column density, can assess whether the extended emission from WR 137 is consistent with dust production from a colliding-wind binary. The inputs required for the geometric dust modeling of WR 137 are the distance ( $d$ ), shock-cone half-opening angle ( $\theta_h$ ), dust expansion velocity ( $v_{\text{exp}}$ ), and orbital parameters of the binary systems, which include the orbital period ( $P_{\text{orb}}$ ), time of periastron passage ( $P_0$ ), inclination ( $i$ ), semimajor axis ( $a$ ), eccentricity ( $e$ ), argument of periastris ( $\omega$ ), the longitude of the ascending node ( $\Omega$ ), and an orbital phase at a given point in time ( $\varphi$ ).

Orbital parameters were adopted from recent CHARA observations with MIRC + CLIMBX that resolved the binary components in WR 137 (N. D. Richardson et al. 2024, in preparation) and also incorporated previous CHARA observations by Richardson et al. (2016). The orbital parameters are provided in Table 2 and assume that the O9 companion star is brighter than the WC7 star in the near-infrared CHARA observations. If instead the WC7 star is assumed to be brighter

**Table 2**  
Properties of the WR 137 Geometric Dust Model

Adopted Properties	
Orbital period ( $P_{\text{orb}}$ )	13.1 yr
Periastron passage date ( $P_0$ )	2023.85
Semimajor axis ( $a$ )	8.56 mas
Eccentricity ( $e$ )	0.315
Inclination ( $i$ )	$97.2^\circ$
Argument of periastris ( $\omega$ )	$0.6^\circ$
Longitude of the ascending node ( $\Omega$ )	$117.91^\circ$
Orbital phase ( $\varphi$ )	0.90
Shock-cone half-opening angle ( $\theta_h$ )	$18.6^\circ$
Distance to WR 137 ( $d$ )	1941 pc
Dust expansion velocity ( $v_{\text{exp}}$ )	$1700 \text{ km s}^{-1}$
Azimuthal dust modulation centroid ( $\mu_{\text{Az}}$ )	$180^\circ$
Free Parameters	
Azimuthal dust modulation width ( $\sigma_{\text{Az}}$ )	$6^\circ$
Orbital dust modulation centroid ( $\mu_{\text{orb}}$ )	$265^\circ$
Orbital dust modulation width ( $\sigma_{\text{orb}}$ )	$13^\circ$

**Note.** The orbital period was adopted from Lefèvre et al. (2005) and N. D. Richardson et al. (2024, in preparation), and the other orbital parameters ( $P_0$ ,  $a$ ,  $e$ ,  $i$ ,  $\omega$ , and  $\Omega$ ) were adopted from recent CHARA observations of WR 137 (N. D. Richardson et al. 2024, in preparation). The dust expansion velocity is assumed to be consistent with the wind velocity of the WC star provided by Richardson et al. (2016), and the half-opening angle is derived from the wind-momentum balance between the WC and companion star (Equation (1) in Richardson et al. 2016). The adopted orbital phase is consistent with the expected orbital phase at the time of the observations, 2022 July 15 (Table 1). The azimuthal dust modulation centroid was assumed to be  $\mu_{\text{Az}} = 0^\circ$ . The remaining three orbital and azimuthal dust modulation parameters ( $\mu_{\text{orb}}$ ,  $\sigma_{\text{orb}}$ , and  $\sigma_{\text{Az}}$ ) were the only free parameters in the model and were adjusted until a satisfactory agreement with the calibrated observables from the F480M observations was achieved (Figure 6, right).

than the O9 companion, there would simply be  $180^\circ$  added to the argument of periastris ( $\omega$ ). The value of  $\omega = 0.6^\circ$ , which assumes the O9 star is brighter than the WC7 star, is notably in closer agreement with the value derived independently from radial velocity observations by Lefèvre et al. (2005;  $\omega = 326^\circ \pm 15^\circ$ ) than when the WC7 star is assumed to be the brighter near-infrared component ( $\omega = 180.6^\circ$ ).

The effects of nonuniform dust formation can be investigated with the geometric models by modulating dust formation across the surface of the shock cone in the orbital and azimuthal<sup>28</sup> directions (see Figure 3 of Han et al. 2022). Orbitally modulated and azimuthally asymmetric dust production was notably inferred in the colliding-wind W-R binary WR 140 (Williams et al. 2009; Han et al. 2022). As in Han et al. (2022), dust-production variability in the orbital and azimuthal directions are each modeled by a Gaussian distribution of dust density as a function of true anomaly and azimuthal angle, respectively. The parameters of modulated dust production are the centroids ( $\mu$ ) and widths ( $\sigma$ ) of the Gaussian functions in the orbital and azimuthal directions. The model images were calculated at a spatial scale of  $10 \text{ mas pixel}^{-1}$ .

An azimuthal centroid of  $\mu_{\text{Az}} = 180^\circ$  was adopted, which corresponds to enhanced dust formation along the orbital plane in the “trailing arm” of the shock cone (Figure 6, left and center). This assumption is based on dust formation in WR 140, where dust emission is enhanced in the trailing arm (Williams et al. 2009;

<sup>28</sup> i.e., perpendicular to the WR-O star axis.

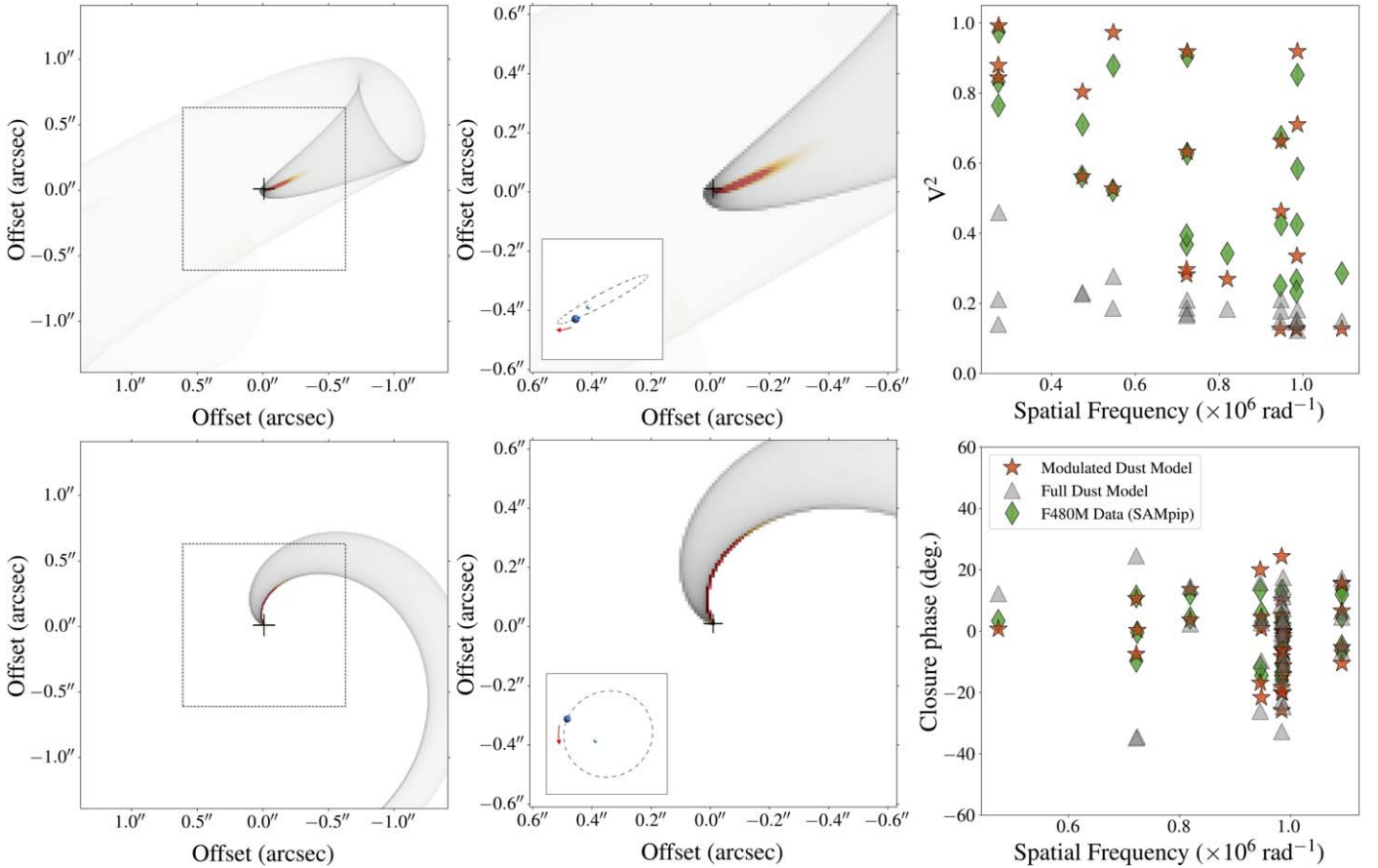


**Figure 6.** Left and center: observed and orbital plane projections of column densities from the full (gray) and modulated (red/orange) geometric dust models of WR 137 using the parameters provided in Table 2 at the orbital phase of the JWST/NIRISS observations ( $\varphi = 0.90$ ). The inset of zoomed images shows the orbit of the O9 star around the WC star at the phase of the JWST/NIRISS observations in the respective projections. The crosses indicate the position of the unresolved binary system. Right: simulated NIRISS AMI squared visibilities and closure phases of the full and modulated dust models compared to the real observables extracted from the F480M data with SAMpip. Observables from the modulated dust model show a closer agreement to the F480M data than the full dust model. Note that the error bars on the F480M observables are smaller than the symbols used.

Han et al. 2022). It is important to note that an asymmetry in dust production between the leading and trailing arms is indeed predicted based on 3D hydrodynamic modeling (Hendrix et al. 2016), however, such models of the colliding-wind binary WR 98a by Hendrix et al. (2016) instead predict dust enhancement in the leading arm. Dust enhancement along the leading arm of WR 137's shock cone (i.e.,  $\mu_{Az} = 0^\circ$ ) cannot be conclusively ruled out due to degeneracies in geometric model parameters. Multiepoch observations resolving the changing dust morphology around WR 137 will be important for resolving these degeneracies and identifying the region of enhanced dust formation.

In order to compare with the NIRISS AMI observations of WR 137, the dust column density maps output from the geometric modeling tool were converted to intensity assuming isothermal and optically thin dust emission. Given the higher signal-to-noise ratio of the F480M observations, the column density maps were converted to intensity at  $4.8 \mu\text{m}$ . Emission from the unresolved binary, which is not incorporated in the geometric models, is included by modifying the central pixel of the dust map output from the geometric modeling tool. Since dust emission is coincident along the line of sight with stellar emission from the binary, it is not possible to distinguish the stellar and dust emission from the NIRISS observations. However, archival mid-infrared light curves that sampled WR 137 throughout its orbit can be used to estimate the

emission from the central binary and circumstellar dust (Williams et al. 2001). The stellar emission at  $4.8 \mu\text{m}$ ,  $F_{4.8\mu\text{m}}^* = 0.8 \text{ Jy}$ , can be derived from the quiescent  $L'$ -band ( $\lambda = 3.8 \mu\text{m}$ ) flux density,  $F_{3.8\mu\text{m}}^* = 1.7 \text{ Jy}$ , and the  $\lambda F_\lambda^* \propto \lambda^{-1.86}$  power law that characterizes the IR spectrum of its quiescent emission (Williams et al. 2001). The total  $4.8 \mu\text{m}$  emission,  $F_{4.8\mu\text{m}}^{\text{Tot}} = 2.8 \text{ Jy}$  is estimated from  $M'$ -band ( $\lambda = 4.7 \mu\text{m}$ ) photometry of WR 137 obtained by Williams et al. (2001) in 1996 March, which corresponds to a similar orbital phase of WR 137 as that of the JWST NIRISS observations ( $\varphi \sim 0.9$ ). The dust column density map and the stellar component were simply scaled to 70% and 30% of  $F_{4.8\mu\text{m}}^{\text{Tot}}$ , respectively, to produce a  $4.8 \mu\text{m}$  intensity model of WR 137.

Synthetic interferometric observables were extracted from the model  $4.8 \mu\text{m}$  intensity maps of WR 137 to compare with the NIRISS F480M observables. Specifically, the F480M observables obtained using SAMpip (Figure 2) were used to compare the synthetic observables. The synthetic observables were extracted by computing the discrete Fourier transform of the model image using the spatial frequencies sampled with NIRISS AMI. From the Fourier amplitudes and phases, the squared visibilities and closure phases were constructed using the baseline information of the NRM. Uncertainties on the synthetic squared visibilities and closure phases were adopted

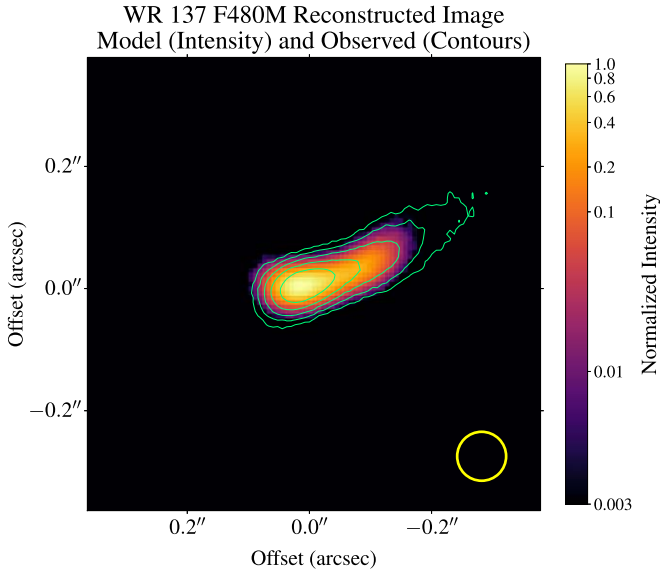


**Figure 7.** SQUEEZE image reconstruction of the modulated dust model with contours of a SQUEEZE-reconstructed image from SAMpip F480M observables. The contour levels correspond to normalized intensities of  $10^{-2.5}$ ,  $10^{-2}$ ,  $10^{-1.5}$ ,  $10^{-1}$ , and  $10^{-0.5}$ . The yellow circle corresponds to the angular resolution of the F480M observations ( $\sim 80$  mas).

from the SAMpip F480M observables. Note that the extraction of synthetic F480M observables assumes a single wavelength ( $\lambda = 4.8 \mu\text{m}$ ) for the dust emission from the model.

With the azimuthal centroid fixed at  $\mu_{Az} = 180^\circ$ , the remaining three free dust modulation parameters ( $\sigma_{Az}$ ,  $\mu_{Orb}$ , and  $\sigma_{Orb}$ ) were adjusted to find a satisfactory agreement with the SAMpip F480M closure phases and squared visibilities. Figure 6 (left and center) presents the dust column density maps from the geometric modeling of WR 137 with and without incorporating the modulated dust-production parameters from Table 2. The interferometric observables of the geometric dust models and the F480M observations presented in Figure 6 (right) show that the observables from the model without modulated dust production disagree with the observations, as expected. Figure 6 (right) demonstrates the general agreement between the observations and the modulated dust-production model where dust production is confined to the orbital plane and is enhanced as the system approaches periastris.

A reconstructed image using SQUEEZE with a similar configuration used for the F480M image reconstruction (see Section 3.1; Figure 4) was generated from the synthetic observables of the modulated geometric dust model. Figure 7 presents a reconstructed image of the modulated dust model overlaid with the contours of the SQUEEZE-reconstructed image from the SAMpip/F480M-calibrated observables (see Figure 4). The morphology and intensity profile of the extended dust emission from the modulated dust model show a close agreement to the F480M observations. This agreement suggests that extended dust emission from WR 137 can be explained by dust production via the colliding-wind mechanism with modulated dust-formation rates along the surface of the shock cone.

#### 4. Discussion: Dust Formation Enabled by Enhanced Equatorial Mass Loss from the O9 Companion?

Observations of persistent double-peaked emission line profiles from the O9 companion star in WR 137 and its

polarization signature indicate that the O9 star has a decretion disk that may be linked to the star’s rapid rotation (Harries et al. 2000; Richardson et al. 2016; St-Louis et al. 2020). The enhancement of dust production along WR 137’s orbital plane (Figure 6) may therefore be influenced by anisotropic wind densities and velocities that differ from those of a nonrotating O star. The polarimetric observations of WR 137 notably indicate the disk is aligned with the orbital plane of the system (Harries et al. 2000; St-Louis et al. 2020). It is therefore plausible that an anisotropic, equatorially enhanced wind from the O9 companion presents more favorable conditions for dust formation via the colliding-wind mechanism along the orbital plane due to enhanced densities. The potential influence of anisotropic winds on colliding-wind dust formation has been observed in another W-R binary, Apep (Callingham et al. 2019; Han et al. 2020). Recent spectroscopic mid-infrared observations of WR 137 with the Stratospheric Observatory for Infrared Astronomy also suggest that the interaction between the WC and O9 winds is important for triggering dust formation (Peatt et al. 2023).

In order to investigate dust-forming conditions in the colliding-wind shock, we utilize the dimensionless parameter,  $\Gamma$ , defined by Usov (1991) to characterize the radiative cooling of gas in the shock layer:

$$\Gamma \simeq 0.8 \left( \frac{\dot{M}_{WR}}{10^{-5} M_{\odot} \text{ yr}^{-1}} \right) \left( \frac{D}{0.67 \text{ au}} \right)^{-1} \left( \frac{v_{WR}}{10^3 \text{ km s}^{-1}} \right)^{-3} \times (1 + \eta^{1/2}) \eta^{1/2}, \quad (3)$$

where  $D$  is the instantaneous separation between the W-R and the companion star and  $\eta$  is the momentum ratio of the companion star wind over that of the W-R star (Equation (2)). Higher values of  $\Gamma$  indicate increased cooling of hot gas in the shock. The radiative cooling efficiency is an important factor in dust formation since the hot  $\sim 10^7$ – $10^8$  K gas must cool to  $\sim 1000$  K in order to form dust. We note that  $\Gamma$  does not account for clumping, which likely plays a significant role in colliding-wind dust formation (Eatson et al. 2022). However, as a simplified investigation of dust formation in colliding winds, we assume that WR 137 forms dust for a range of  $\Gamma$  values similar to the values of  $\Gamma$  derived from dust-formation episodes of WR 140. WR 140 is a well-studied, dust-forming colliding-wind binary, which forms dust at a phase interval  $\varphi_{\text{dust}} = \pm 0.04$  around periastron passage (Han et al. 2022). Based on Equation (3) and adopting stellar and orbital properties of WR 140 from previous literature, we calculate  $\Gamma$  for WR 140,  $\Gamma_{WR140}$ , and normalize by  $\Gamma$  at the separation where WR 140’s dust formation begins/ends,  $D_{\text{dust}} = 8.3 \text{ au}$ .<sup>29</sup>

$$\frac{\Gamma_{WR140}(D)}{\Gamma_{WR140}(D_{\text{dust}})} = 1.0 \left( \frac{D}{8.3 \text{ au}} \right)^{-1}. \quad (4)$$

We adopt a W-R mass-loss rate, terminal wind velocity, and OB/WR wind-momentum ratio of  $\dot{M}_{WR} = 2 \times 10^{-5}$  (Sugawara et al. 2015),  $v_{WR} = 2860 \text{ km s}^{-1}$  (Williams & Eenens 1989), and  $\eta = 0.043$  (Han et al. 2022) for WR 140, respectively.

It is important to emphasize that utilizing  $\Gamma$  as a dust-formation diagnostic does not capture all of the complex physics of dust condensation in colliding winds. For example,

<sup>29</sup> Assuming the Gaia distance to WR 140 of 1.64 kpc (Thomas et al. 2021).

although  $\Gamma_{\text{WR140}}$  increases as WR 140 approaches periastron ( $\varphi = 0$ ;  $D = 1.5$  au), observations demonstrate that dust formation at separation distances  $D < D_{\text{dust}}$  appears to *decrease* relative to  $D = D_{\text{dust}}$  (Williams et al. 2009; Han et al. 2022). When the stars are close, “sudden radiative braking” of the W-R wind due to deceleration by photospheric UV emission of the O star (Gayley et al. 1997) likely plays an important role in mitigating dust production at close separations. However, an investigation of these effects is beyond the scope of this work.

Using the orbital parameters of WR 137 from Table 2 and the mass-loss rates and terminal wind velocities from Richardson et al. (2016), we can calculate  $\Gamma_{\text{WR137}}$  normalized by  $\Gamma_{\text{WR140}}(D_{\text{dust}})$  as follows:

$$\frac{\Gamma_{\text{WR137}}(D)}{\Gamma_{\text{WR140}}(D_{\text{dust}})} = 0.82 \left( \frac{D}{13.2 \text{ au}} \right)^{-1}, \quad (5)$$

where  $D = 13.2$  au corresponds to the binary separation in WR 137 at the time of the JWST observations at an orbital phase of  $\varphi = 0.90$ .

A comparison of  $\Gamma/\Gamma_{\text{WR140}}(D_{\text{dust}})$  for WR 140 and WR 137 throughout the stellar separation of their respective orbits is shown in Figure 8. Despite the clear evidence for dust production at the time of the JWST observations (Figure 3 and 4), Figure 8 suggests that throughout its entire orbit, the radiative cooling of shocked gas in WR 137 is not strong enough to allow for dust production with the adopted stellar and orbital properties. However, the adopted mass-loss rates and wind velocities of WR 137 (Richardson et al. 2016) were derived assuming spherical symmetry and thus do not account for enhanced equatorial mass loss from the O-star companion. Interestingly, Maeder & Meynet (2000) predict that the equatorial mass-loss rate is enhanced by a factor of  $\sim 2$  for a rapidly rotating O star (see Table 1 of Maeder & Meynet 2000). If the mass-loss rate and/or terminal wind velocity of the companion O star in WR 137 were enhanced by a factor of 2, the radiative cooling in the colliding winds would satisfy the dust-formation threshold at the stellar separation at the time of the JWST observations (Figure 8).

We note that the isotropic O-star mass-loss rates from Richardson et al. (2016) have large uncertainties ( $\log \dot{M} = -7.1_{-0.3}^{+1.0}$ ) so that the upper limit would allow dust to form. However, a larger isotropic mass-loss rate from the O star would also lead to a larger value of  $\eta$  and a wider shock-cone opening angle (see Equation (1)), which is not consistent with the linear morphology of the dust emission in the NIRISS observations (Figures 3 and 4). We therefore argue that colliding-wind dust production in WR 137 is enabled by enhanced equatorial mass loss from the O9 companion. Rapid stellar rotation may therefore promote dust production in colliding-wind binaries, and circumstellar dust emission confined to the orbital and/or equatorial plane of the rapidly rotating star likely indicates the impact of this effect.

It is important to address the following caveats on the interpretations and discussion. The analysis of dust-forming conditions using the  $\Gamma$  parameter notably does not consider a possible reduction in the mass-loss rate or wind velocity that would impact the wind-momentum ratio  $\eta$ . Asymmetric winds would also alter the morphology of the colliding-wind shock cone that would deviate from the geometric model presented in Figure 6. Additionally, it is unclear if rapid stellar rotation can result in enhanced mass loss confined to such a narrow angular region ( $\sim 6^\circ$ ; Table 2) around the equator. Future work with

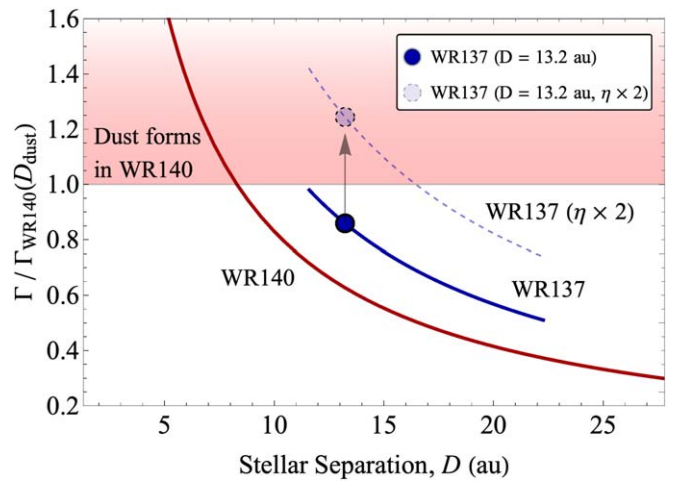


**Figure 8.** Estimated colliding-wind dust-formation thresholds for WR 137 and WR 140 as a function of binary separation,  $D$ , using the dimensionless radiative cooling efficiency parameter,  $\Gamma$ , as a diagnostic.  $\Gamma$  is normalized by the value when dust formation begins/ends in WR 140,  $\Gamma_{\text{WR140}}(D_{\text{dust}} = 8.3 \text{ au})$ . The shaded region above  $\Gamma/\Gamma_{\text{WR140}}(D_{\text{dust}}) = 1$  corresponds to where dust formation is expected based on observations of WR 140 and its orbital parameters; however, note that other factors such as sudden radiative braking may inhibit dust production at close separation distance where  $\Gamma/\Gamma_{\text{WR140}}(D_{\text{dust}}) \gg 1$ . WR 137 may not be expected to form dust unless the wind-momentum ratio of its O-star companion to the WC star,  $\eta$  (Equation (2)), is enhanced by a factor of  $\sim 2$  due to a rapidly rotating O-star companion (e.g., Maeder & Meynet 2000).

hydrodynamical simulations (e.g., Eatson et al. 2022) that can capture the complex physics of colliding-wind dust formation with asymmetric wind(s) will be important for investigating if nonspherical mass loss can indeed promote dust production in colliding-wind binaries

## 5. Summary

In this paper, we presented JWST observations of the periodic dust-forming colliding-wind binary system WR 137 using the AMI mode of NIRISS with the F380M and F480M filters. The observations were taken as part of the WR DustERS program (ERS 1349) and provide some of the first science results using the NIRISS AMI observing mode on JWST. Notably, the WR 137 results demonstrate that NIRISS AMI is uniquely suited for observations of faint and extended mid-infrared emission around a bright central core at angular scales of  $\lesssim 400$  mas. The NIRISS AMI observations of WR 137 were obtained with two different dither strategies (see Section 2). The analysis in this work was performed on the “stare” (nondithered) observations.

We extracted interferometric observables from the interferogram pattern from the WR 137 observations and calibrated against a PSF calibrator star (HD 228337) using three different software packages: ImPlaneIA, SAMpip, and AMICAL. The calibrated squared visibilities of the WR 137 observations were consistent across all three software packages (Figure 2). The calibrated closure phases from AMICAL and SAMpip were consistent as well, while closure phases derived from ImPlaneIA were slightly discrepant. The cause for the discrepant closure phases is currently under investigation. The F480M observations yielded observables with the smallest uncertainties, which is likely due to the larger number of NGROUPS in each integration than in the F380M integrations (Table 1).

Images of WR 137 were reconstructed from the interferometric observables using three different software tools: BSMEM, SQUEEZE, and IRBis. Each tool utilized the three sets of observables extracted from the three software packages. The reconstructed F380M and F480M images presented a nearly identical picture of WR 137 with a bright central core and with a  $\sim 200$ – $300$  mas quasi-linear filament extending toward the northwest (Figures 3 and 4). The similarity of the images reconstructed with these three independent tools demonstrates the robustness of capturing WR 137’s morphology from the NIRISS AMI observations.

The expected half-opening angle of the shock cone in WR 137 is  $\theta_h = 18.6^\circ$  (see Section 3.3), but a shock cone that wide is not consistent with the linear morphology of the resolved dust emission. We used the geometric colliding-wind dust modeling tool from Han et al. (2022) to interpret the linear dust morphology extending from WR 137 using orbital parameters from recent CHARA observations by N. D. Richardson et al. (2024, in preparation; Table 2). In order to reproduce the linear appearance of the extended dust emission, variable dust-production rates across the surface of the colliding-wind shock cone in the orbital and azimuthal directions were needed. A geometric model with dust formation confined to the orbital plane and enhanced as the system approaches periastron provided a closer agreement to the interferometric observables from the F480M observations than the full model without any dust-production variability (Figure 6). An image reconstructed by SQUEEZE from the modulated dust-model observables showed a close resemblance to the reconstructed image from the F480M observations (Figure 7).

We discussed the possible effect of enhanced equatorial mass loss from the O9 companion star in WR 137 (Richardson et al. 2016; St-Louis et al. 2020) to explain the linear morphology of the observed dust production. We used the analytical colliding-wind dust-production framework by Usov (1991) and the well-studied orbital and stellar properties of WR 140 as a reference to investigate dust formation in WR 137. As a diagnostic for dust formation in colliding winds, we used estimated values of the parameter  $\Gamma$ , which characterizes the radiative cooling of gas in the colliding-wind shock layer (Usov 1991). We found that WR 137 should not be capable of forming dust given its orbital and stellar properties (Figure 8). However, if the equatorial mass loss from the rapidly rotating O9 companion star were enhanced by a factor of  $\sim 2$  (Maeder & Meynet 2000), this would be sufficient to enable dust formation in WR 137 (Figure 8). We therefore conclude that equatorially enhanced mass loss from the rapidly rotating O9 companion star may be responsible for the dust formed along the orbital plane of WR 137, which is aligned with the rotation axis of the O9 star (St-Louis et al. 2020).

JWST observations of WR 137 with NIRISS AMI provided us with the necessary imaging contrast and sensitivity at mid-infrared wavelengths to perform a morphological analysis of dust-forming conditions in colliding winds. Our results present a first look at the capabilities of NIRISS AMI that indicate its potential for investigating a wide range of astrophysical environments having bright central cores and faint and close-in extended emission, including active galactic nuclei, evolved stars, and young stellar objects. Notably, the dynamic range of NIRISS AMI observations is expected to improve as technical studies progress for optimizing the analysis and calibration of these data sets, which will allow for probing even fainter

features (see Ray et al. 2023; Sallum et al. 2024). Subpixel dithering (Fruchter & Hook 2002) and improved calibration of second-order systematics such as charge migration may also bring F380M and F430M data up to the quality seen in F480M (see Section 3.1). In this work, our aim was not only to investigate colliding-wind dust production, but also to provide a first look at science with the NIRISS AMI observing mode on JWST and to set the stage for the future of space-based aperture-masking observations.

### Acknowledgments











R.M.L. would like to acknowledge the members of the entire W-R DustERS team for their valuable discussions and contributions to this work. We thank Amaya Moro-Martin, William Januszewski, Neill Reid, Margaret Meixner, and Bonnie Meinke for their support of the planning and execution of our DD-ERS program. We would also like to acknowledge the NIRISS instrument and MIRaGe teams for their support of our observation preparation and data analysis plans. We also thank Tomer Shenar for the correspondence on the stellar wind models of WR 137. We would also like to acknowledge the anonymous referee for the insightful feedback that has improved the quality and clarity of this work. A.F.J.M. is grateful to NSERC (Canada) for financial aid. N.D.R. is grateful for support from the Cottrell Scholar Award #CS-CSA-2023-143 sponsored by the Research Corporation for Science Advancement. J.S.-B. acknowledges the support received from the UNAM PAPIIT project IA 105023; and from the CONAHCyT “Ciencia de Frontera” project CF-2019/263975.




This work is based on observations made with the NASA/ESA/CSA James Webb Space Telescope. The data were obtained from the Mikulski Archive for Space Telescopes at the Space Telescope Science Institute, which is operated by the Association of Universities for Research in Astronomy, Inc., under NASA contract NAS 5-03127 for JWST. These observations are associated with program #1349. Support for program #1349 was provided by NASA through a grant from the Space Telescope Science Institute, which is operated by the Association of Universities for Research in Astronomy, Inc., under NASA contract NAS 5-03127. The material is based upon work supported by NASA under award No. 80GSFC21M0002.

All of the data presented in this paper were obtained from the Mikulski Archive for Space Telescopes (MAST) at the Space Telescope Science Institute. The specific observations analyzed can be accessed via DOI:10.17909/ytb0-px48.

Facility: JWST/NIRISS.

### ORCID iDs

Ryan M. Lau  <https://orcid.org/0000-0003-0778-0321>  
 Matthew J. Hankins  <https://orcid.org/0000-0001-9315-8437>  
 Joel Sanchez-Bermudez  <https://orcid.org/0000-0002-9723-0421>  
 Deepashri Thatte  <https://orcid.org/0000-0002-1536-7193>  
 Anthony Soulain  <https://orcid.org/0000-0001-7661-5130>  
 Rachel A. Cooper  <https://orcid.org/0000-0001-7864-308X>  
 Anand Sivaramakrishnan  <https://orcid.org/0000-0003-1251-4124>  
 Michael F. Corcoran  <https://orcid.org/0000-0002-7762-3172>  
 Olivia C. Jones  <https://orcid.org/0000-0003-4870-5547>  
 Thomas Madura  <https://orcid.org/0000-0001-7697-2955>

Mark R. Morris  <https://orcid.org/0000-0002-6753-2066>  
 Noel D. Richardson  <https://orcid.org/0000-0002-2806-9339>  
 Nathan Smith  <https://orcid.org/0000-0001-5510-2424>  
 Peter Tuthill  <https://orcid.org/0000-0001-7026-6291>  
 Gerd Weigelt  <https://orcid.org/0000-0001-9754-2233>  
 Peredur M. Williams  <https://orcid.org/0000-0002-8092-980X>

## References

- Allen, D. A., Swings, J. P., & Harvey, P. M. 1972, *A&A*, **20**, 333  
 Artigau, É., Sivaramakrishnan, A., Greenbaum, A. Z., et al. 2014, *Proc. SPIE*, **9143**, 914340  
 Baron, F., Monnier, J. D., & Kloppenborg, B. 2010, *Proc. SPIE*, **7734**, 77342I  
 Buscher, D. F. 1994, in IAU Symp. 158, Very High Angular Resolution Imaging, ed. J. G. Robertson & W. J. Tango (Dordrecht: Kluwer), **91**  
 Callingham, J. R., Tuthill, P. G., Pope, B. J. S., et al. 2019, *NatAs*, **3**, 82  
 Cantó, J., Raga, A. C., & Wilkin, F. P. 1996, *ApJ*, **469**, 729  
 Coulton, W. R., Armstrong, R., Smith, K. M., Lupton, R. H., & Spergel, D. N. 2018, *AJ*, **155**, 258  
 Crowther, P. A. 2007, *ARA&A*, **45**, 177  
 Doyon, R., Willott, C. J., Hutchings, J. B., et al. 2023, *PASP*, **135**, 098001  
 Duvert, G., Young, J., & Hummel, C. A. 2017, *A&A*, **597**, A8  
 Eatson, J. W., Pittard, J. M., & Van Loo, S. 2022, *MNRAS*, **516**, 6132  
 Fruchter, A. S., & Hook, R. N. 2002, *PASP*, **114**, 144  
 Gayley, K. G., Owocki, S. P., & Cranmer, S. R. 1997, *ApJ*, **475**, 786  
 Greenbaum, A. Z., Pueyo, L., Sivaramakrishnan, A., & Lacour, S. 2015, *ApJ*, **798**, 68  
 Greenbaum, A. Z., Sivaramakrishnan, A., Sahlmann, J., & Thatte, D. 2018, ImPlaneIA: Image Plane Approach to Interferometric Analysis, Astrophysics Source Code Library, ascl:1808.004  
 Hamann, W. R., & Gräfenor, G. 2004, *A&A*, **427**, 697  
 Hamann, W. R., Gräfenor, G., Liermann, A., et al. 2019, *A&A*, **625**, A57  
 Han, Y., Tuthill, P. G., Lau, R. M., et al. 2020, *MNRAS*, **498**, 5604  
 Han, Y., Tuthill, P. G., Lau, R. M., & Soulain, A. 2022, *Natur*, **610**, 269  
 Hankins, M. J., Lau, R. M., Morris, M. R., et al. 2016, *ApJ*, **827**, 136  
 Harries, T. J., Babler, B. L., & Fox, G. K. 2000, *A&A*, **361**, 273  
 Hendrix, T., Keppens, R., van Marle, A. J., et al. 2016, *MNRAS*, **460**, 3975  
 Hilbert, B., Sahlmann, J., Volk, K., et al. 2022, MIRaGe: Multi Instrument Ramp Generator, Astrophysics Source Code Library, ascl:2203.008  
 Hirata, C. M., & Choi, A. 2020, *PASP*, **132**, 014501  
 Hofmann, K. H., Weigelt, G., & Schertl, D. 2014, *A&A*, **565**, A48  
 Lau, R. M., Eldridge, J. J., Hankins, M. J., et al. 2020a, *ApJ*, **898**, 74  
 Lau, R. M., Hankins, M. J., Han, Y., et al. 2020b, *ApJ*, **900**, 190  
 Lau, R. M., Hankins, M. J., Han, Y., et al. 2022, *NatAs*, **6**, 1308  
 Lawson, P. R., Cotton, W. D., Hummel, C. A., et al. 2004, *Proc. SPIE*, **5491**, 886  
 Lefèvre, L., Marchenko, S. V., Lépine, S., et al. 2005, *MNRAS*, **360**, 141  
 Maeder, A., & Meynet, G. 2000, *A&A*, **361**, 159  
 Marchenko, S. V., & Moffat, A. F. J. 2007, in ASP Conf. Ser. 367, Massive Stars in Interactive Binaries, ed. N. St.-Louis & A. F. J. Moffat (San Francisco, CA: ASP), **213**  
 Marchenko, S. V., Moffat, A. F. J., & Grosdidier, Y. 1999, *ApJ*, **522**, 433  
 Monnier, J. D., Tuthill, P. G., Danchi, W. C., Murphy, N., & Harries, T. J. 2007, *ApJ*, **655**, 1033  
 Pauls, T. A., Young, J. S., Cotton, W. D., & Monnier, J. D. 2005, *PASP*, **117**, 1255  
 Peatt, M. J., Richardson, N. D., Williams, P. M., et al. 2023, *ApJ*, **956**, 109  
 Rajagopal, J., Menut, J. L., Wallace, D., et al. 2007, *ApJ*, **671**, 2017  
 Ray, S., Sallum, S., Hinkley, S., et al. 2023, arXiv:2310.11508  
 Richardson, N. D., Shenar, T., Roy-Loubier, O., et al. 2016, *MNRAS*, **461**, 4115  
 Rigby, J., Perrin, M., McElwain, M., et al. 2023, *PASP*, **135**, 048001  
 Sallum, S., Ray, S., Kammerer, J., et al. 2024, *ApJL*, **963**, L2  
 Sanchez-Bermudez, J., Alberdi, A., Schödel, R., & Sivaramakrishnan, A. 2022, *Proc. SPIE*, **12183**, 121831K  
 Sander, A. A. C., Hamann, W. R., Todt, H., et al. 2019, *A&A*, **621**, A92  
 Sivaramakrishnan, A., Tuthill, P., Lloyd, J. P., et al. 2023, *PASP*, **135**, 015003  
 Sivaramakrishnan, A., Tuthill, P., Martinache, F., et al. 2009, Planetary System, Star Formation, and Black Hole Science with Non-redundant Masking on Space Telescopes, Astro2010: The Astronomy and Astrophysics Decadal Survey, Technology Development Papers, NASA, **40**  
 Soulain, A., & Robert, C. M. T. 2023, AMICAL: Aperture Masking Interferometry Calibration and Analysis Library, Astrophysics Source Code Library, ascl:2302.021  
 Soulain, A., Sivaramakrishnan, A., Tuthill, P., et al. 2020, *Proc. SPIE*, **11446**, 1144611  
 St.-Louis, N., Piaulet, C., Richardson, N. D., et al. 2020, *MNRAS*, **497**, 4448  
 Sugawara, Y., Maeda, Y., Tsuboi, Y., et al. 2015, *PASJ*, **67**, 121  
 Thomas, J. D., Richardson, N. D., Eldridge, J. J., et al. 2021, *MNRAS*, **504**, 5221  
 Tuthill, P. G., Monnier, J. D., & Danchi, W. C. 1999, *Natur*, **398**, 487  
 Tuthill, P. G., Monnier, J. D., Lawrence, N., et al. 2008, *ApJ*, **675**, 698  
 Usov, V. V. 1991, *MNRAS*, **252**, 49  
 Williams, P. M. 2019, *MNRAS*, **488**, 1282  
 Williams, P. M., & Eenens, P. R. J. 1989, *MNRAS*, **240**, 445  
 Williams, P. M., Kidger, M. R., van der Hucht, K. A., et al. 2001, *MNRAS*, **324**, 156  
 Williams, P. M., Longmore, A. J., van der Hucht, K. A., et al. 1985, *MNRAS*, **215**, 23P  
 Williams, P. M., Marchenko, S. V., Marston, A. P., et al. 2009, *MNRAS*, **395**, 1749  
 Williams, P. M., van der Hucht, K. A., & Thé, P. S. 1987, *A&A*, **182**, 91